Laser-induced spallation of minerals common on asteroids

Anthony, Niklas

2021-05

Anthony , N , Frostevarg , J , Suhonen , H , Wanhainen , C & Granvik , M 2021 , '
Laser-induced spallation of minerals common on asteroids ' , Acta Astronautica , vol. 182 ,
pp. 325-331 . https://doi.org/10.1016/j.actaastro.2021.02.018

http://hdl.handle.net/10138/332750
https://doi.org/10.1016/j.actaastro.2021.02.018

Acta Astronautica 182 (2021) 325–331

Contents lists available at ScienceDirect

Acta Astronautica

journal homepage: www.elsevier.com/locate/actaastro

Research paper

Laser-induced spallation of minerals common on asteroids

Niklas Anthony [a,*], Jan Frostevarg [b], Heikki Suhonen [c], Christina Wanhainen [d], Mikael Granvik [a,c]

[a] Asteroid Engineering Laboratory, Onboard Space Systems, Luleå University of Technology, Box 848, 98128 Kiruna, Sweden
[b] Department of Engineering Sciences and Mathematics, Luleå University of Technology, 97187, Luleå, Sweden
[c] Department of Physics, P.O. Box 64, 00014 University of Helsinki, Finland
[d] Division of Geosciences and Environmental Engineering, Luleå University of Technology, 97187 Luleå, Sweden

ARTICLE INFO

Keywords:
Laser spallation
High-Speed Imaging
Asteroid redirection
X-ray microtomography

ABSTRACT

The ability to deflect dangerous small bodies in the Solar System or redirect profitable ones is a necessary and worthwhile challenge. One well-studied method to accomplish this is laser ablation, where solid surface material sublimates, and the escaping gas creates a momentum exchange. Alternatively, laser-induced spallation and sputtering could be a more efficient means of deflection, yet little research has studied these processes in detail. We used a 15-kW Ytterbium fiber laser on samples of olivine, pyroxene, and serpentine (minerals commonly found on asteroids) to induce spallation. We observed the process with a high-speed camera and illumination laser, and used X-ray micro-tomography to measure the size of the holes produced by the laser to determine material removal efficiency. We found that pyroxene will spallate at power densities between 1.5 and 6.0 kW cm^{-2}, serpentine will also spallate at 13.7 kW cm^{-2}, but olivine does not spallate at 1.5 kW cm^{-2} and higher power densities melt the sample. Laser-induced spallation of pyroxene and serpentine can be two- to three-times more energy efficient (volume removed per unit of absorbed energy) than laser-induced spattering, and over 40x more efficient than laser ablation.

1. Introduction

Laser ablation is the process of using a laser to heat a small area of material beyond its sublimation temperature, which removes surface material in gas form. The first mention of using laser ablation to alter the orbits of objects in space was in 1994 [1], roughly the same time the US Congress passed its first mandate to NASA to catalogue large near-Earth asteroids (NEAs) and identify potentially hazardous ones. The same process can also be used to de-spin or de-tumble an asteroid to prepare it for processing or manipulation [2]. Asteroid impacts pose a serious threat to the Earth's ecosystem. The mass-extinction event that occurred ~65 million years ago was due to a 10–80-km-diameter asteroid impacting just off the Yucatán peninsula [3]. A more recent (and better-documented) example was the Chelyabinsk superbolide: an NEA roughly 20 m in diameter, traveling over 19 km s^{-1} with respect to the Earth, exploded in the sky near the Russian town of Chelyabinsk in early 2013 [4]. The effects of the explosion (i.e. glass breaking, knocking people and things down, etc.) injured over 1000 people and damaged over 3000 buildings. The famous Tunguska event was most likely caused by a 60-m-diameter object exploding a few kilometers above the forest in the Siberian wilderness [5]. It is vital that we develop technologies and systems capable of mitigating these types of threats.

The profile of a space mission to deflect a potentially hazardous object depends on a number of factors such as warning time, object size, composition, and structure. For relatively short warning times, impulsive methods such as kinetic impact, e.g., NASA's upcoming Double Asteroid Redirection Test (DART) mission, or nuclear blast would be applicable, whereas if more warning time is given, slower methods such as gravity tractor or laser ablation could be used [6]. The slower methods allow for more precise orbit control, which could also open the door for resource exploitation. A recent comparative analysis studied several methods and analyzed their effectiveness at delivering asteroids between 20 and 150 m in diameter to the Earth–Moon system (EMS) [7]. It included ion beam push, tugboat, gravity tractor, laser ablation, and mass driver. Each method has its advantages and disadvantages, such as spacecraft mass, mission duration, and robustness. Using a laser to redirect an asteroid has three advantages: (1) it can be performed without landing, (2) it does not require extra fuel, and (3) it can be used on a variety of targets.

Several challenges arise when building a laser ablation asteroid redirection model. First, all astronomical bodies are rotating or tumbling. A simple fix to account for this was mentioned in [8] where a lateral velocity requires an increase in power density to maintain an appropriate heating time per unit volume. Second, laser beams have

* Corresponding author.
E-mail addresses: niklas.anthony@ltu.se (N. Anthony), mgranvik@iki.fi (M. Granvik).

https://doi.org/10.1016/j.actaastro.2021.02.018
Received 3 December 2020; Received in revised form 11 February 2021; Accepted 14 February 2021
Available online 23 February 2021

divergence, and are thus very sensitive to focal length. While some models, like that in [9], mention the effects of this sensitivity, most assume perfect spot control. Even if the spot is perfectly maintained, the issues surrounding beam divergence will re-emerge as the hole gets deeper. Third, unless the laser is operating in the femtosecond pulse range, thermal effects will cause a melt front to appear given enough time [10].

Over 80% of the known NEAs are S-type or C-type, composed of mostly silicates and carbonaceous materials, respectively [11]. It is suggested that olivine and pyroxene make up the bulk material in these asteroids, and were thus selected for study [12]. As water is one of the most speculative space resources, serpentine was chosen to be studied as well, as it is the most common hydrated mineral found in meteorites [13]. Laboratory experiments with laser ablation have been performed in the context of asteroid redirection. Some studied the effects of a continuous-wave, 90-W laser on an olivine sample in a vacuum chamber [14,15]. Force measurements on pyroxene as well as high-fidelity asteroid simulant powders were also performed with a 33-W average power, picosecond pulsed laser [16]. The DE-STAR system has been developed over the past six years, and have studied the effects of a phased-array laser system on basalt [17].

The fundamentals of laser cutting and drilling were outlined in 1964, just four years after the invention of the laser [18]. These processes have been drastically improved over the decades with the addition of assist gases and new laser sources. High-Speed Imaging (HSI) has also allowed researchers to observe the processes that occur during laser irradiation, e.g. melt pool behavior [19] and spatter dynamics [20] (when molten material is ejected from the melt pool), as well as the effects of processing gases [21]. It has recently been shown that, using a 300-W laser, minerals like olivine, pyroxene, and serpentine will liquefy and sputter a significant amount of material well before a steady-state vapor "engine" forms [22]. Some research suggests that an even more efficient mechanism of material removal is spallation, where solid pieces of material break off without melting [23]. The study showed that for sandstone and slate, the power density that caused spallation (just before melting) was the most energy efficient, which is a crucial factor when considering spacecraft mass and power requirements. Here we seek to answer questions like: Will olivine, pyroxene, and/or serpentine exhibit spallation behavior? What laser parameters (i.e. power and pulse width) will produce spallation? Is the energy efficiency comparable to previous work in [22] and [23]?

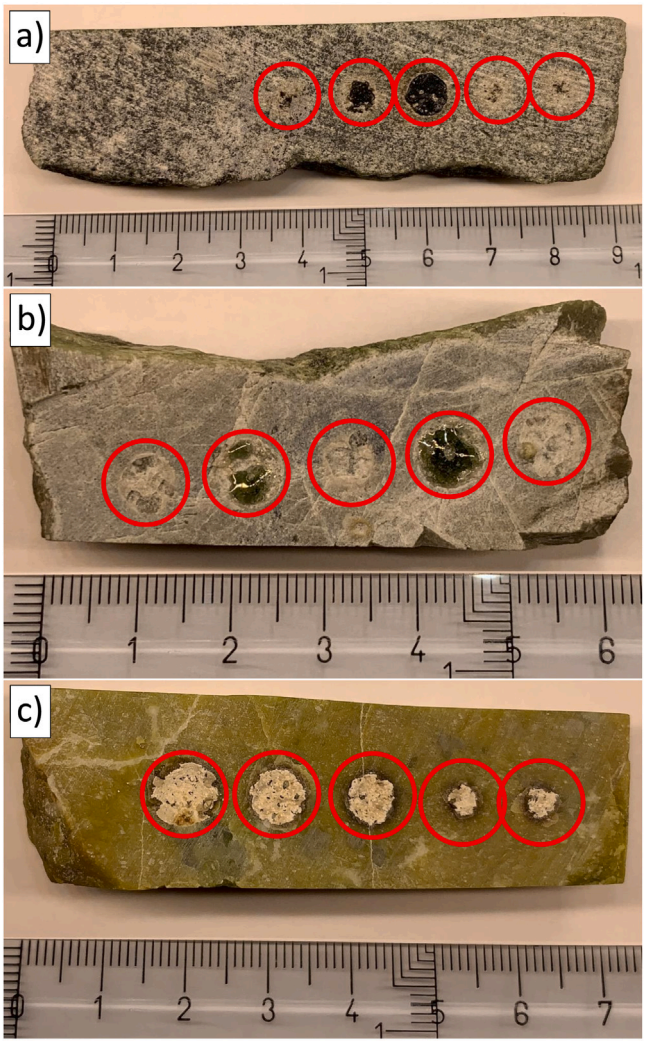

Fig. 1. Images of the pre-characterized samples showing overall macroscopic characteristics; from top to bottom, they are: (a) olivine, (b) pyroxene, and (c) serpentine. The red circles indicate the location of experiments. The units on the ruler are cm.

2. Methodology

First, two samples each of olivine, pyroxene, and serpentine were cut into roughly 1-cm thick pieces. The source rocks were the same as the pre-characterized samples used in [22]. One sample of each mineral was pre-analyzed with X-ray microtomography (XMT), the other samples were used more experimentally to find promising laser pulse parameters, which would then be used on the pre-analyzed samples. Each experiment, both on the testing and pre-characterized samples, was recorded with a setup consisting of a high-speed camera and an illumination laser. All of the samples were then analyzed with XMT to characterize the resulting cavities.

2.1. Sample characterization

As the samples used in this experiment were cut from the same source as in previous research, we will assume that the mineralogical and spectroscopic properties are the same as found in [22]. In summary, the petrographic analysis revealed that the pyroxene and serpentine samples show more variation than the olivine sample, meaning they have larger regions of differing compositions and clear boundaries between the regions. It also revealed that the pyroxene and serpentine had more cracks and cleavages compared to olivine. The spectroscopic analysis revealed that, at the wavelength of the laser, our serpentine sample was the most reflective (28%), followed by pyroxene (22%) and olivine (19.5%). Images of the samples were taken after the experiments, and are shown in Fig. 1.

The density of olivine, pyroxene, and serpentine are 3.8 g cm^{-3}, 3.4 g cm^{-3}, and 2.6 g cm^{-3}, respectively [24].

2.2. Laser experiment and observation

The experiments were conducted with a YLR-15000-MM-WC Ytterbium fiber laser from IPG Photonics, with capabilities given in Table 1. The laser head (using mirror optics) was fixed to a crossbar and angled 15° from horizontal to prevent reflections from damaging the optics. Argon gas flowing at 20 L min^{-1} was used as a shielding gas. The target was placed on a one-dimensional platform in order to move the sample between experiments. The surfaces of the samples were placed beyond the focal plane, such that it created a 1-cm-diameter spot, allowing for power densities up to 13.7 kW cm^{-2}. The beam profile in focus was a top-hat shape, but out of focus it more resembled a Gaussian shape.

The High-Speed Imaging (HSI) system used in these experiments was based on the setup in [19]. A high-speed camera (FASTCAM Mini UX100 type 800-M-16G) was operated at 12 500 fps at a resolution of 1024x400 to capture what physical processes occurred during laser irradiation. A 810 nm bandpass filter was used in conjunction with an

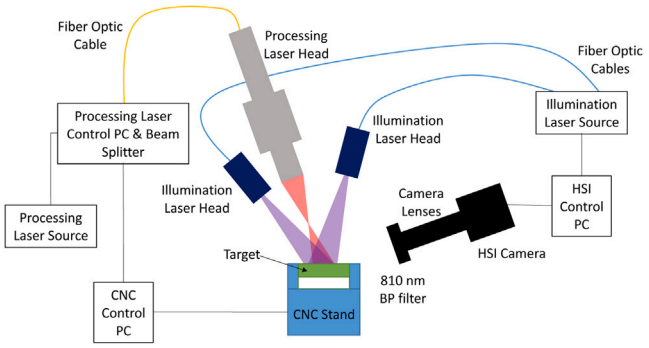

Fig. 2. Experiment setup.

Table 1
Laser parameters.

Parameter	Value
Wavelength	1070 nm
Source power	<15 000 W
Min. pulse length	1 ms
Core diameter	200 μm
Beam quality	10.5 mm mrad

Table 2
Parameter space used.

Parameter	Value
Power (kW)	1.5, 3.0, 4.5, 5.0, 6.0 6.5, 9.0, 11.7, 12.7, 13.7
Pulse width (ms)	5, 10, 20, 30, 35
Pulse gap (ms)	1, 5, 10, 20, 100

illumination laser of the same wavelength (CaviLux CW) in order to filter out most of the processing light, thereby providing a clearer view of the experiment sites. The illumination laser was split into two optical heads (30 W each). The HSI camera used an exposure time of 62.5 μs per frame. An overview of the entire experiment setup is given in Fig. 2.

There were three independent variables in the experiments: laser power, pulse width, and pulse gap. We configured the laser control PC to produce the exact number of pulses required. The power varied from 1 500 W to 13 659 W, the pulse widths from 5 ms to 35 ms, and the pulse gaps from 1 to 100 ms; the exact values are given in Table 2. The maximum output power of the laser was limited due to damaged modules, so 13 659 W was the highest power setting possible.

The parameter selection began with the olivine test sample, as it had the most surface area to experiment on. The experiments began with the lowest power setting of 1.5 kW and a pulse width of 10 ms; the HSI footage was studied immediately after. Based on the results, the power was incrementally increased until melting just started to happen. This procedure was repeated for the other two test samples to find the power density that produced spallation before melting. Using these power densities, the pulse widths and powers were varied while maintaining the total pulse energy (e.g., halving the power required doubling the pulse length) to see if that had any effect on the results. Each sample had at least one experiment where a train of 5 pulses were sent in succession to see if more spallation would occur or if melting would dominate.

The pulse parameters were manually entered into the processing laser control PC. The CNC PC was used to toggle the shielding gas and processing laser via an ethernet connection. The recording on the HSI PC was manually activated after the CNC PC program was started. The HSI PC triggered the illumination laser and HSI camera to capture two seconds of footage. The resulting recording was analyzed, clipped, and saved to include only the part of the file where processing and cooling occurred. The manual capture method was successful in 33 out of 34 experiments.

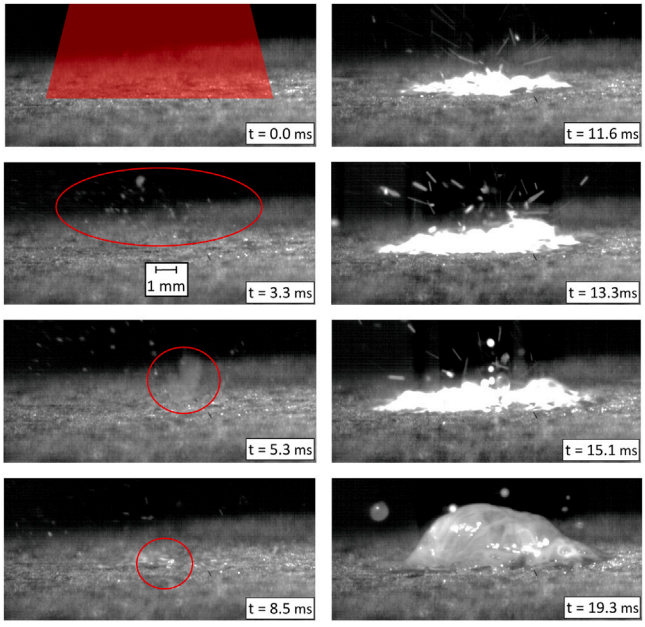

Fig. 3. Frames from HSI of laser irradiation on olivine. The laser power was 5 kW and pulse length of 20 ms. Time flows from top to bottom, starting in the left column. The laser spot size is shown in the top left frame, spallation is seen at 3.3 ms, a hyperfast jet at 5.3 ms, and the sputtering processes begins at 8.5 ms. The bottom right frame shows the melt pool cooling as the laser is shut off.

2.3. X-ray microtomography

The XMT measurements were carried out with a GE phoenix nanotom s system. The generator settings were 100 kV and 150 μA and a 0.5 mm Cu filter was added to the beam. A total number of 1000 projections over 360 degree rotation with 3 x 500 ms exposure time were recorded to pre-characterize the samples, and 1200 projections with 1 x 500 ms exposure time were made on the post-processed samples. A voxel size of 33 μm or 40 μm was chosen for each scan. The 3D volume data was reconstructed from these data sets using datos|x reconstruction software version 2.4.0.1199 (GE phoenix).

3. Results

The results are split into two sections: the HSI observation of the processing, and the XMT measurements.

3.1. Laser irradiation and high-speed imaging

Olivine shows weak spallation at the powers used in the experiments. Initially, some small (micrometer-sized) pieces come off (up until 5.3 ms in Fig. 3), and soon the area at the center of the laser beam begins to melt and sputter (at 8.5 ms in Fig. 3). As the irradiation continues, the size of the melt pool increases, eventually matching the laser spot diameter of 1 cm. The size of the spatter also increases, some pieces over 1 mm in diameter. One unique feature of the olivine experiment was, what appear to be, hyper-fast jets that lasted only one frame (5.3 ms in Fig. 3) before the melting began. These jets were roughly 1 mm in width, and visible 2–3 mm above the surface. Once the laser was shut off, a large, translucent mass of bubbles formed over the irradiated area (up to 4 mm in height), possibly filled with gas from the olivine sample, and/or a combination of the shielding gas and atmosphere.

Pyroxene, the next mineral to be tested, behaved notably different compared to olivine. The initial moments of the laser irradiation caused the pyroxene to become lighter (from 0.0 to 2.0 ms in Fig. 4). The

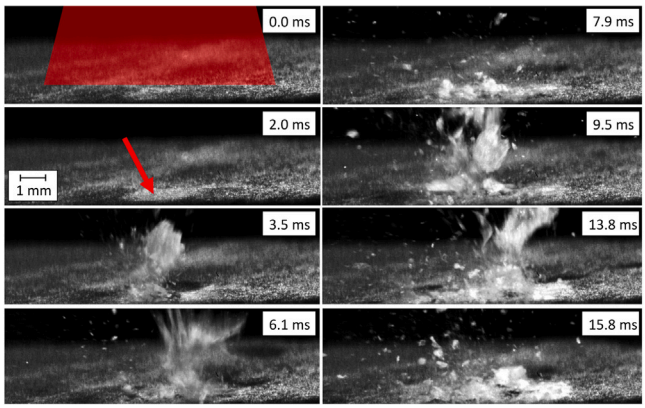

Fig. 4. Frames from HSI of laser irradiation on pyroxene. The laser power was 3 kW and pulse length was 20 ms. Arrow in the 2.0 ms frame highlights the discoloration prior to spallation.

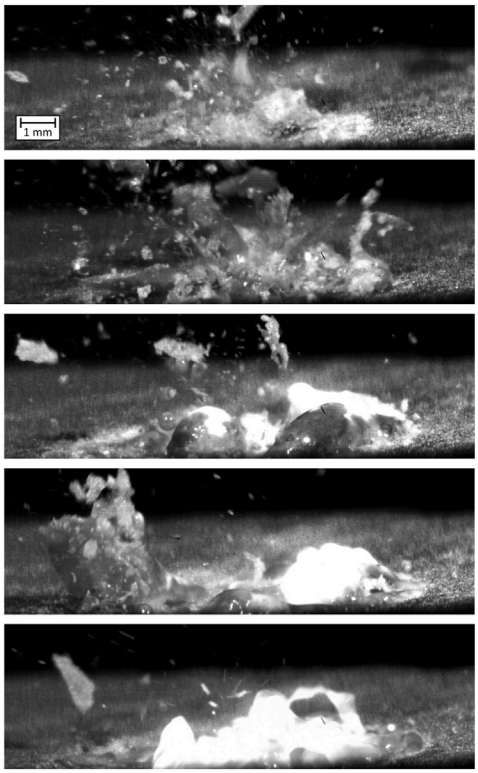

Fig. 5. Frames from HSI of laser irradiation on pyroxene. Each frame is taken from the middle of each pulse in a 5-pulse experiment. The laser power was 3 kW, pulse width was 20 ms, and the pulse gaps were 100 ms.

discoloration continued until spallation began. The pieces ranged in size from less than 1 μm to 4–5 mm. Throughout the experiment, areas of the pyroxene under irradiation would become lighter and then spallate. As the total energy of the experiment began to increase (i.e., more pulses were used) the pyroxene began to melt, and exhibited spattering behavior similar to that of olivine (Fig. 5). Of the five experiments, the ones with one pulse were dominated by spallation; clips from the HSI of these experiments can be seen in Supplementary Videos 1 (Hole 1 in Table 3), 2 (Hole 3 in Table 3) and 3 (Hole 5 in Table 3).

Serpentine behaved similar to pyroxene, though it required significantly more energy to begin the process. The laser had to be turned up to the maximum power and use longer pulse lengths than those

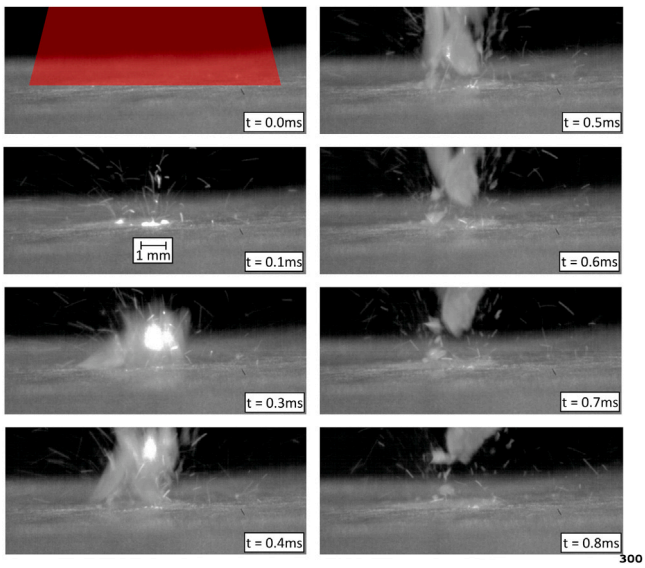

Fig. 6. Frames from HSI of laser irradiation on serpentine. The power is 12.4 kW and pulse length is 20 ms. This figure captures a spallation event within the first millisecond of exposure.

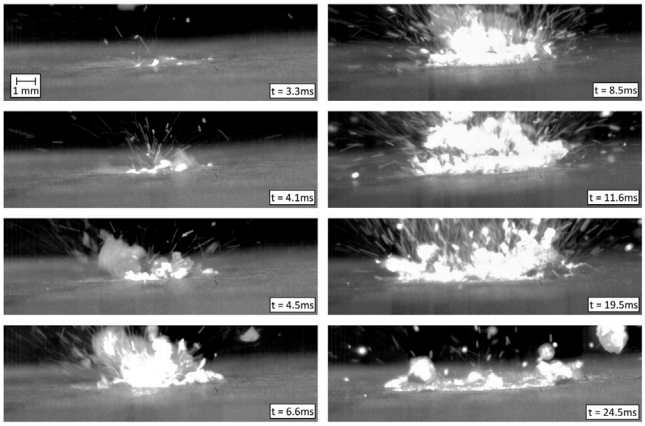

Fig. 7. Frames from HSI of laser irradiation on serpentine. The power is 12.4 kW and the pulse length is 20 ms. This figure shows the spallation and sputtering of the entire pulse, including some after-effects seen at 24.5 ms. Note this is footage from the same experiment as Fig. 6.

used for both olivine and pyroxene. The processing began similar to that of pyroxene, except the material darkened instead of lightened (Fig. 6). The area under the center of the laser beam began to melt and sputter sub-μm pieces until several large (1–2 mm), flat chunks came off. After the initial spallation, the sputtering of sub-μm pieces continued and grew. As time progressed, a combination of molten and solid chunks ranging from sub-μm to 2 mm continued to break off (up to 6.6 ms in Fig. 7). A relatively large piece (4–5 mm in width) can be seen breaking off behind the spatter at 8.5 ms. As the processing area began to match the laser spot diameter (~1 cm), the processing was dominated by what looked to be a more molten-sputtering scenario, though some spallation of millimeter-sized pieces still occurred. The melt pool behaved differently than for olivine and pyroxene. There was no one large pool that chaotically threw off material, rather a more steady stream of molten material being cast off as small pieces directly from the surface (from 8.5 to 19.5 ms in Fig. 7). A clip of the HSI where both spallation and spattering is present is given in Supplementary Videos 4 (Hole 1 in Table 3).

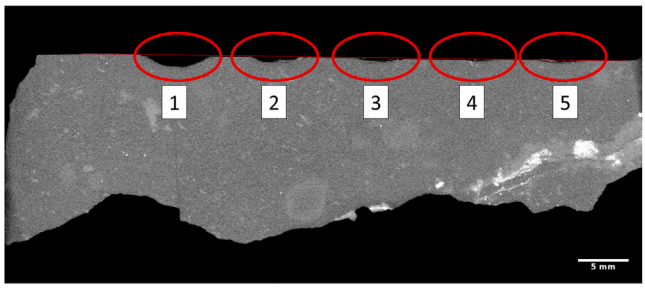

Fig. 8. A cross-section image from the XMT scan of the serpentine sample post-processing. The surface is designated with a thin line, and the five experiments are circled.

3.2. X-ray microtomography analysis

As the holes were shallow and material began to extrude above the hole edges, calculating the volume was a challenge. Unfortunately, accurate values of volume removed could only be extracted from the pre-characterized samples. The 3D volume data was analyzed using the free software Fiji (ImageJ) [25,26] by first manually choosing a small region of interest (ROI) around each hole (see Fig. 8. First the pre-image and post-image were resampled to the same voxel size (33 μm or 40 μm) if necessary. Then the 3D images were aligned using Fijiyama plugin (version 2020-09-02) [27]. The gray scale of the pre-image was normalized so that its mean and standard deviation matched those of the post-image. Then for each ROI to be analyzed the aligned pre- and post-images were subtracted from each other to create a difference image. Prior to subtraction, the pre-images were displaced with sub-pixel accuracy along the sample surface normal to make the subtraction as accurate as possible. The best displacement was chosen such that the standard deviation of the difference image would be minimized at the surface location at the edges of the ROI (away from the hole). A threshold value was then chosen as $T = (v_{\mathrm{rock}} - v_{\mathrm{air}})/3$, where v_{rock} and v_{air} are the gray levels of rock material and air in the pre-image. The difference image was then segmented to into two parts: first, the hole (values below $-T$), and second, material that had re-solidified on top of the surface (values above $+T$). An outlier removal with radius of 2 pixels was run on the individual slices of the segmented data, and further a volume opening with the minimum voxel count of 100 was applied to the 3D segmented data. The volumes of the segmented components were directly calculated from the data. The errors for the volume calculations were estimated as the standard deviation of the volumes when the subtraction was done with different displacements of the pre-images along the sample surface normal (range ±1 pixel).

A summary of the volume of material removed for each experiment is given with its measurement standard deviation in Table 3. The measured volume removed is given with a standard deviation, which was calculated by varying the surface plane height. The total energy is found by multiplying the pulse power (from the laser) by the absorptivity of the material at the laser's wavelength determined in [22]. Volume efficiency is found by dividing the volume removed by the total energy (with unit conversion). Mass rate represents the volume removal rate, and it was calculated by dividing the volume removed by the length of the pulses and multiplying by the material density. The ranges accompanying the volume efficiency and mass rate are based on the standard deviation of the volume removed.

4. Discussion

The spot size of the laser beam was sufficiently large as to average out any micro-structural differences, which led to a large variation in the results reported in [22]. The images of the holes (Fig. 1) show a consistent color among the olivine and pyroxene, though there seems to be a difference between the test and control samples of serpentine. The test sample shows the darkening feature of the initial exposure to laser irradiation, as the power levels were too low to initiate melting or spallation. The control sample has a consistently white color in all the samples, with perhaps a darkened ring on the right two sites. These rings are due to the shape of the laser profile being Gaussian (i.e. high power in the center, reducing radially.)

Due to the fact the target was placed beyond the focal point of the laser, the laser power intensity grew the further above the surface the pieces traveled, thus solid material moving upwards would show signs of melting.

The spallation seen in the olivine experiments was possibly not even due to the olivine mineral, rather local concentration of other minerals like pyroxene, that do easily spallate. This can be seen in the two right-most circles in Fig. 1, as well as on the test pieces; the laser would "remove" the darker spots, leaving a lighter circle. Pyroxene was also the only material of the three tested that did not completely melt. If material can be removed without melting, the freshly-exposed and un-altered material can be compared to that on the original surface, to study the effects of space weathering.

The presence of processed material poses a challenge to the spacecraft environment. Even the earliest mention of ablation-related deflection mention that the re-deposition of gas on the solar concentrator would limit the mission to 10–30 minutes [28]. For laser systems, the gas would coat the solar panels and focusing optics, making them less efficient or breaking them completely. If the processed material is instead broken into macroscopic pieces, it changes the resulting environment around the spacecraft. Although there may still be some gas, most of the material will be relatively slow-moving particles, and thus will not accumulate on vital components.

When looking at the streaks produced by spatter in Figs. 3 and 7, we can estimate the velocity of the fastest moving particles. The streaks are roughly 1 mm long, which, divided by the camera exposure time of 62.5 μs, gives us a velocity of 16 m s^{-1}. The larger chunks move more slowly, roughly 8 m s^{-1}, which is still faster than the escape velocity of an 11.5-km-diameter spherical asteroid (assuming a density of 3 g cm^{-3}). It must be noted that these values are derived from one 2-D view, and the velocities can vary depending on their movement towards or away from the camera. The velocity derived from the streak can also vary depending on the size of the particle, though these ranges are not expected to exceed one order of magnitude.

Due to the small size of the sample pieces, they tended to heat up after some of the longer or higher-powered experiments. This could be due to low thermal conductivity compared to, say, metals. It may be beneficial to perform laser processing on the night side of an asteroid, as re-radiation of heat from the laser is more efficient.

The majority of holes (12 out of 15) had some material pushed up around the edges, or re-solidified on the surface. Only three pyroxene holes had no measurable material above the surface. The material that formed the edges is subtracted from our estimate for the volume removed to provide a more accurate estimate of the total volume that escaped the sample. The correction does not affect the results for pyroxene or serpentine much, but it does have a strong effect on experiments with olivine, because the estimate for the volume removed would otherwise often be negative. In such cases we assume that the laser irradiation sublimated or vaporized some material which became trapped in the melt pool, and reported that the experiment did not remove any material.

The highest volume processing efficiencies previously found in [22] were 25.2, 36.7, and 23.2 mm^3 kJ^{-1} for olivine, pyroxene, and serpentine, respectively, at power densities up to 900 kW cm^{-2}. The highest values found in this work were 14.8, 63.3, and 63.9 mm^3 kJ^{-1} for olivine, pyroxene, and serpentine, respectively at power densities as low as 1.4 kW cm^{-2}. For reference, the volume removal efficiencies estimated in [14] were around 1 mm^3 kJ^{-1}, and the values found in [23] were over 1968 mm^3 kJ^{-1}. Both cases operated in the same

Table 3
Volume removed as found by XMT analysis. Also shown are the calculated volume removal efficiencies and mass removal rate.

	Hole Nr.	Volume Removed (mm^3)	Power (W)	Pulse Length (ms)	Pulses	Total Energy (J)	Volume Efficiency (mm^3 kJ^{-1})	Mass Rate (g s^{-1})
Olivine	1	0.004 ± 0.007	3,000	10	1	24.2	0.2 ± 0.3	0.002 ± 0.003
	2	0.014 ± 0.009	1,500	20	1	24.2	0.6 ± 0.4	0.003 ± 0.002
	3	1.783 ± 1.003	3,000	10	5	120.8	14.8 ± 8.3	0.136 ± 0.076
	4	0.076 ± 0.050	5,000	10	1	40.3	1.9 ± 1.2	0.029 ± 0.019
	5	0.286 ± 0.442	3,000	20	1	48.3	5.9 ± 9.2	0.054 ± 0.084
Pyroxene	1	2.964 ± 1.092	6,000	10	1	46.8	63.3 ± 23.3	1.008 ± 0.415
	2	5.503 ± 0.604	6,000	10	5	234.0	23.5 ± 2.6	0.374 ± 0.046
	3	1.908 ± 0.579	3,000	20	1	46.8	40.8 ± 12.4	0.324 ± 0.110
	4	7.788 ± 0.888	3,000	20	5	234.0	33.3 ± 3.8	0.265 ± 0.034
	5	2.468 ± 0.819	1,500	35	1	41.0	60.3 ± 20.0	0.240 ± 0.089
Serpentine	1	18.845 ± 1.012	13,659	30	1	295.0	63.9 ± 3.4	1.602 ± 0.128
	2	4.926 ± 0.538	13,659	20	1	196.7	25.0 ± 2.7	0.628 ± 0.102
	3	2.031 ± 0.459	13,659	10	2	196.7	10.3 ± 2.3	0.259 ± 0.087
	4	0.254 ± 0.132	13,166	10	2	189.6	1.3 ± 0.7	0.032 ± 0.025
	5	0.870 ± 0.237	6,820	20	2	196.4	4.4 ± 1.2	0.055 ± 0.023

power density region as the experiments in this paper (between 784 and 13659 W/cm^2). In the first case, the experiment (on an olivine sample) was allowed to run for 10 min, with the explicit purpose of entering a solid-state vapor mode, which would explain the low processing efficiency. The second case was very efficient, as the targets were sandstone and shale, very brittle rocks, which spallate relatively easily; for instance, sandstone contains mostly the mineral quartz.

The HSI footage of the olivine experiments showed that besides a few microscopic flakes, the material did not spallate at any of the tested laser parameters. The material removal process was dominated by molten-sputtering. For pyroxene, the three single-pulse cases were clearly dominated by spallation. The five-pulse cases began with spallation, but quickly became dominated by sputtering after the first pulse. It is difficult to state clearly which process dominates for serpentine, as our only tool of analysis is the HSI. There are clearly large pieces that remain solid throughout their removal, especially in the first few milliseconds, but bright spatter eventually fills the field of view. Experiment #1 for serpentine has a volume removal efficiency over twice that of sputtering-driven experiments in [22], so we suggest that for that experiment, spallation was the driving process.

The highest mass removal rate found in [22] was 0.041 g s^{-1}, and the highest found in this current work was 1.602 g s^{-1}, an increase of over one and a half orders of magnitude. For reference, the estimated mass removal rate in [17] was roughly 0.016 g s^{-1}, and in [14] was roughly (0.0001 g s^{-1}). This again, has important implications for asteroid redirection. In order to maintain a gas plume, control of both the spot location and the focal plane would require extremely precise GNC equipment, perhaps two systems (one for the laser and one for the spacecraft) [2]. Our research suggests that, due to the time scale difference between spallation/spattering and ablation, these requirements can be relaxed, and the laser spot instead *should* be allowed to wander within limits, spallating and spattering new material, as opposed to creating a vapor jet.

The reported mass rate represents the material removal rate, which cannot be directly equated with momentum exchange, which, in turn, is relevant when considering asteroid redirection. A second path of research would need to be opened to analyze the net "thrust" generated by spallation and spatter, in addition to the thermodynamic model. A challenge there lies in the fact that we do not know the exact density of the molten material coming off of the sample, and how it changes as it cools, possibly trapping gas within it. The spallation and spatter seem to extend a full 180 degrees (also reported in [14]).

The processing performance degrades for pyroxene and serpentine when using multiple pulses. The performance degradation could be due to the material cooling back down, and the beginning segments of future pulses simply re-heat the material instead of processing it. In olivine, the multiple-pulse case was instead the most energy efficient, which could be due to the fact that it had sufficient energy to put it into the molten-spattering mode, which gives values closer to those found in previous work [22].

Serpentine contains hydroxyl (OH) groups that are located between layers of SiO_4 tetrahedra and AlO_6 octahedra. The relatively high pulse energies required to process the material could be due to the OH absorbing and dissipating energy from the hole area. Both the serpentine and pyroxene samples had characteristic cleavages, which could explain why they spallate better than olivine.

In pyroxene, two experiments can be compared: case 1 and 3, where the energies are the same, but the pulse parameters differ slightly. It appears the shorter, more powerful pulse processes the material more efficiently. On the other hand, case 5 suggests that a long, low-power pulse processes material nearly as effectively as case 1. It is possible that all three cases process material equally efficiently, as the error bars do overlap.

Building a thermodynamic model that includes spallation, spattering, and ablation will prove to be challenging. Existing laser ablation models (such as the one in [15]) include factors like specific heat, phase change enthalpies, and radiative and conductive losses. Spallation/spattering is noted, but not included in the model. One would have to determine what percentages of the total material removed is due to each process (spallation/spattering/ablation). This also does not include the energy absorbed by hydroxyl and water in hydrated minerals; a real asteroid may not consist of pure minerals, but a heterogeneous mix of minerals, metals, and volatiles.

5. Conclusions

The research presented above sought to answer the following questions: do olivine, pyroxene, and serpentine exhibit spallation behavior? If so, what power densities and pulse parameters seem to produce the most energy efficient spallation behavior? How does laser-induced spallation perform relative to laser-induced spattering or ablation? After carrying out the experiments, observing them with HSI, and measuring the hole sizes with XMT, a number of conclusions can be drawn:

1. The HSI revealed that olivine does not tend to spallate at power densities between 1.5 and 13.7 kW cm^{-2}, whereas pyroxene and serpentine will do so. It is important to have a good estimate of the surface composition of an asteroid before considering using laser-induced spallation for redirection.
2. The XMT analysis showed that processing pyroxene and serpentine at power densities between 1.5 and 13.7 kW cm^{-2} yielded volume-removal efficiencies of over 60 mm^3 kJ^{-1}. This is two- to three-times more energy efficient than laser-induced spattering, and over 40 times more energy efficient than laser ablation.

3. A new laser-based asteroid redirection/detumbling model should be developed to include spallation and spattering in addition to ablation. The new energy efficiency may allow for a smaller/lighter laser, fewer solar panels, and leaner GNC system requirements.

Declaration of competing interest

The authors declare that they have no known competing financial interests or personal relationships that could have appeared to influence the work reported in this paper.

Acknowledgments

This research was partly funded by the Knut and Alice Wallenberg Foundation, Sweden, and used services of the X-ray Micro-CT Laboratory at the Department of Physics, University of Helsinki.

Appendix A. Supplementary data

Supplementary material related to this article can be found online at https://doi.org/10.1016/j.actaastro.2021.02.018.

References

[1] C.R. Phipps, M.M. Michaelis, NEO-LISP: Deflecting near-earth objects using high average power, repetitively pulsed lasers, 1994, pp. 19–23, Presented at the ECLIM 23: Laser Interaction With Matter.
[2] M. Vetrisano, C. Colombo, M. Vasile, Asteroid rotation and orbit control via laser ablation, Adv. Space Res. 57 (8) (2016) 1762–1782, Advances in Asteroid and Space Debris Science and Technology - Part 2.
[3] P. Schulte, L. Alegret, I. Arenillas, J.A. Arz, P.J. Barton, P.R. Bown, T.J. Bralower, G.L. Christeson, P. Claeys, C.S. Cockell, G.S. Collins, A. Deutsch, T.J. Goldin, K. Goto, J.M. Grajales-Nishimura, R.A.F. Grieve, S.P.S. Gulick, K.R. Johnson, W. Kiessling, C. Koeberl, D.A. Kring, K.G. MacLeod, T. Matsui, J. Melosh, A. Montanari, J.V. Morgan, C.R. Neal, D.J. Nichols, R.D. Norris, E. Pierazzo, G. Ravizza, M. Rebolledo-Vieyra, W.U. Reimold, E. Robin, T. Salge, R.P. Speijer, A.R. Sweet, J. Urrutia-Fucugauchi, V. Vajda, M.T. Whalen, P.S. Willumsen, The chicxulub asteroid impact and mass extinction at the cretaceous-paleogene boundary, Science 327 (5970) (2010) 1214.
[4] O.P. Popova, P. Jenniskens, V. Emel'yanenko, A. Kartashova, E. Biryukov, S. Khaibrakhmanov, V. Shuvalov, Y. Rybnov, A. Dudorov, V.I. Grokhovsky, D.D. Badyukov, Q.-Z. Yin, P.S. Gural, J. Albers, M. Granvik, L.G. Evers, J. Kuiper, V. Kharlamov, A. Solovyov, Y.S. Rusakov, S. Korotkiy, I. Serdyuk, A.V. Korochantsev, M.Y. Larionov, D. Glazachev, A.E. Mayer, G. Gisler, S.V. Gladkovsky, J. Wimpenny, M.E. Sanborn, A. Yamakawa, K.L. Verosub, D.J. Rowland, S. Roeske, N.W. Botto, J.M. Friedrich, M.E. Zolensky, L. Le, D. Ross, K. Ziegler, T. Nakamura, I. Ahn, J.I. Lee, Q. Zhou, X.-H. Li, Q.-L. Li, Y. Liu, G.-Q. Tang, T. Hiroi, D. Sears, I.A. Weinstein, A.S. Vokhmintsev, A.V. Ishchenko, P. Schmitt-Kopplin, N. Hertkorn, K. Nagao, M.K. Haba, M. Komatsu, T. Mikouchi, Chelyabinsk airburst, damage assessment, meteorite recovery, and characterization, Science 342 (6162) (2013) 1069–1073.
[5] C.F. Chyba, P.J. Thomas, K.J. Zahnle, The 1908 Tunguska explosion: atmospheric disruption of a stony asteroid, Nature 361 (6407) (1993) 40–44.
[6] C. Gritzner, K. Dürfeld, J. Kasper, S. Fasoulas, The asteroid and comet impact hazard: risk assessment and mitigation options, Naturwissenschaften 93 (8) (2006) 361–373.
[7] M.C.F. Bazzocchi, M.R. Emami, Comparative analysis of redirection methods for asteroid resource exploitation, Acta Astronaut. 120 (2016) 1–19.
[8] N. Thiry, M. Vasile, Theoretical peak performance and optical constraints for the deflection of an S-type asteroid with a continuous wave laser, Adv. Space Res. 59 (5) (2017) 1353–1367.
[9] R. Kahle, E. Kührt, G. Hahn, J. Knollenberg, Physical limits of solar collectors in deflecting Earth-threatening asteroids, Aerosp. Sci. Technol. 10 (3) (2006) 256–263.
[10] M. Sabsabi, Chapter 7 - femtosecond LIBS, in: J.P. Singh, S.N. Thakur (Eds.), Laser-Induced Breakdown Spectroscopy, Elsevier, Amsterdam, 2007, pp. 151–171.
[11] R.P. Binzel, F.E. DeMeo, E.V. Turtelboom, S.J. Bus, A. Tokunaga, T.H. Burbine, C. Lantz, D. Polishook, B. Carry, A. Morbidelli, M. Birlan, P. Vernazza, B.J. Burt, N. Moskovitz, S.M. Slivan, C.A. Thomas, A.S. Rivkin, M.D. Hicks, T. Dunn, V. Reddy, J.A. Sanchez, M. Granvik, T. Kohout, Compositional distributions and evolutionary processes for the near-earth object population: Results from the MIT-hawaii near-earth object spectroscopic survey (MITHNEOS), Icarus 324 (2019) 41–76.
[12] V. Reddy, T.L. Dunn, C.A. Thomas, N.A. Moskovitz, T.H. Burbine, Mineralogy and surface composition of asteroids, in: P. Michel, F.E. DeMeo, W.F. Bottke (Eds.), Asteroids IV, 2015, pp. 43–63.
[13] A.E. Rubin, Mineralogy of meteorite groups, Meteorit. Planet. Sci. 32 (1997) 231–247.
[14] A. Gibbings, M. Vasile, I. Watson, J.-M. Hopkins, D. Burns, Experimental analysis of laser ablated plumes for asteroid deflection and exploitation, Acta Astronaut. 90 (1) (2013) 85–97, NEO Planetary Defense: From Threat to Action - Selected Papers from the 2011 IAA Planetary Defense Conference.
[15] M. Vasile, A. Gibbings, I. Watson, J.-M. Hopkins, Improved laser ablation model for asteroid deflection, Acta Astronaut. 103 (2014) 382–394.
[16] J. Sloane, Laser ablation propulsion of asteroids with a sub-nanosecond pulsed laser (PhD thesis), University of Maryland, College Park, 2019.
[17] P. Lubin, G.B. Hughes, J.J. Bible, J. Bublitz, J. Arriola, C. Motta, J. Suen, I. Johansson, J. Riley, N. Sarvian, D. Clayton-Warwick, J. Wu, A. Milich, M. Oleson, M. Pryor, P. Krogen, M. Kangas, H. O'Neill, Toward directed energy planetary defense, Opt. Eng. 53 (2) (2014) 1–19.
[18] C.M. Adams, G.A. Hardway, Fundamentals of laser beam machining and drilling, IEEE Trans. Ind. Gen. Appl. IGA-1 (2) (1965) 90–96.
[19] J. Pocorni, J. Powell, J. Frostevarg, A.F.H. Kaplan, Investigation of the piercing process in laser cutting of stainless steel, J. Laser Appl. 29 (2) (2017) 022201–1–022201–8.
[20] D.K.Y. Low, L. Li, P.J. Byrd, The effects of process parameters on spatter deposition in laser percussion drilling, Opt. Laser Technol. 32 (5) (2000) 347–354.
[21] M. Schneider, L. Berthe, R. Fabbro, M. Muller, M. Nivard, Gas investigation for laser drilling, J. Laser Appl. 19 (3) (2007) 165–169.
[22] N. Anthony, J. Frostevarg, H. Suhonen, C. Wanhainen, A. Penttilä, M. Granvik, Laser processing of minerals common on asteroids, Opt. Laser Technol. (2020) 106724.
[23] Z. Xu, C.B. Reed, G. Konercki, R.A. Parker, B.C. Gahan, S. Batarseh, R.M. Graves, H. Figueroa, N. Skinner, Specific energy for pulsed laser rock drilling, J. Laser Appl. 15 (1) (2003) 25–30.
[24] F. Deer, W. A., R.A. Howie, J. Zussman, An Introduction to the Rock-Forming Minerals, Mineralogical Society of Great Britain and Ireland, 2013.
[25] C.T. Rueden, J. Schindelin, M.C. Hiner, B.E. DeZonia, A.E. Walter, et al., ImageJ2: ImageJ for the next generation of scientific image data, BMC Bioinformatics 18 (2017) 529.
[26] J. Schindelin, I. Arganda-Carreras, E. Frise, V. Kaynig, M. Longair, T. Pietzsch, S. Preibisch, C. Rueden, S. Saalfeld, B. Schmid, J.-Y. Tinevez, D.J. White, V. Hartenstein, K. Eliceiri, P. Tomancak, A. Cardona, Fiji: an open-source platform for biological-image analysis, Nat. Methods 9 (7) (2012) 676–682.
[27] R. Fernandez, C. Moisy, Fijiyama: a registration tool for 3D multimodal time-lapse imaging, Bioinformatics (2020) btaa846.
[28] H.J. Melosh, Solar asteroid diversion, Nature 366 (6450) (1993) 21–22.